



## Research Paper

# Oxygen vacancy-rich 2D/2D BiOCl-g-C<sub>3</sub>N<sub>4</sub> ultrathin heterostructure nanosheets for enhanced visible-light-driven photocatalytic activity in environmental remediation



Qiao Wang<sup>a</sup>, Wei Wang<sup>a,\*</sup>, Lingling Zhong<sup>a</sup>, Dongmei Liu<sup>a</sup>, Xingzhong Cao<sup>b</sup>, Fuyi Cui<sup>a,\*</sup>

<sup>a</sup> State Key Laboratory of Urban Water Resource and Environment (SKLUWRE), School of Municipal and Environmental Engineering, Harbin Institute of Technology, Harbin 150090, PR China

<sup>b</sup> Multi-discipline Research Division, Institute of High Energy Physics, Chinese Academy of Sciences, Beijing 100049, China

## ARTICLE INFO

## Keywords:

Oxygen vacancy  
2D/2D heterostructure  
Ultrathin nanosheets  
Photocatalysis

## ABSTRACT

Photocatalytic degradation has been unearthed as a promising strategy for environmental remediation, and the calling is endless for more efficient photocatalytic system. In this study, a novel oxygen vacancy-rich two-dimensional/two-dimensional (2D/2D) BiOCl-g-C<sub>3</sub>N<sub>4</sub> ultrathin heterostructure nanosheet (CN-BC) is successfully prepared by a facile solvothermal method for degradation of non-dye organic contaminants. HRTEM observes the formation of heterojunction, while ESR and XPS unveil the distinct oxygen vacancy concentrations. Density functional calculations reveal that the introduction of oxygen vacancies (OVs) brings a new defect level, resulting in the increased photoabsorption. Under visible light irradiation, the OVs-rich optimum ratio of CN-BC (50CN-50BC) Exhibits 95% removal efficiency of 4-chlorophenol within 2 h, which is about 12.5, 5.3 and 3.4 times as that of pure BiOCl, g-C<sub>3</sub>N<sub>4</sub> and OVs-poor heterostructure, respectively. The photocatalytic mechanism of OVs-rich 50CN-50BC is also revealed, suggesting that the synergistic effect between 2D/2D heterojunction and oxygen vacancies greatly promotes visible-light photoabsorption and photoinduced carrier separation efficiency with a prolonged lifetime, which is confirmed by multiple optical and electrochemical analyses, including DRS, steady-state photoluminescence spectra, electrochemical impedance spectroscopy, photocurrent response and time-resolved fluorescence spectra. This study could bring new opportunities for the rational design of highly efficient photocatalysts by combining 2D/2D heterojunctions with oxygen vacancies in environmental remediation.

## 1. Introduction

Semiconductor photocatalysis technology has been considered to be a green and benign method to eliminate most environmental contaminations [1]. Thus, exploiting high-efficient and environment-friendly visible-light-driven photocatalysts has attracted explosive attention due to their potential application in solar energy conversion [2–4]. Among various photocatalysts investigated, triggered by the great success of graphene, two-dimensional (2D) nanosheets have emerged as a new class of photocatalysts, which benefit from their large specific surface areas and unique structural feature of ultimate two-dimensional anisotropy with small thickness. These characters can increase intimate surface to contact with reactants, shorten the transmission path of the photoinduced charges and realize the effective separation of electron-hole pairs [5,6]. When the thickness of the bulk materials is reduced to nanometer and even subnanometer scale, the

surface atomic structures such as coordination number, bond length, and degree of atom disorder will vary [7]. The ultrathin nanosheets will lead to a large fraction of exposed interior atoms and inevitably induce the formation of various defects with structure disorder on the surface, which can enhance the optical absorption and serve as highly active sites for photocatalytic reactions, inducing a nonnegligible enhancement on the photocatalytic activity [7–9]. Thus, ultrathin 2D nanosheets have been regarded as a new opportunity to synthesize highly efficient photocatalysts.

Bismuth oxychloride (BiOCl), a new type of promising layered materials for photocatalytic environmental remediation, has been intensively investigated due to its stabilized chemical property, non-toxicity, corrosion resistance, indirect-transition band gap and open crystalline structure [10–12]. The indirect-transition band gap of BiOCl forces the excited electron to travel a certain k-space distance to the valence band (VB), which reduces the recombination probability of the

\* Corresponding authors.

E-mail addresses: [wangweirs@hit.edu.cn](mailto:wangweirs@hit.edu.cn), [psweiwang@aliyun.com](mailto:psweiwang@aliyun.com) (W. Wang), [cuifuyi@hit.edu.cn](mailto:cuifuyi@hit.edu.cn) (F. Cui).

excited electron and the hole [13]. On the other hand, BiOCl has an open layered structure consisting of  $[Bi_2O_2]^{2+}$  layers sandwiched between two slabs of halogen ions, which provides a large space to polarize the related atoms and orbitals, and then enhances the separation of the photoinduced electron-hole pairs [14]. However, despite these excellent advantages, BiOCl is limited by its wide band gap, making it useful only under UV irradiation, which results in its poor visible-light photocatalytic performance. Up to now, many strategies have been employed to regulate and modify BiOCl, such as morphological control [15,16], exposure of specific crystal faces [11,17], and heterologous hybridization [18], however, the acquired visible-light photoactivity is generally active in dye photosensitization degradation, and the photocatalytic performance is unsatisfactory [17,19]. Recently, Xie et al. [20] has synthesized triple-vacancy BiOCl ultrathin nanosheets, which had highly photocatalytic efficiency for Rhodamine B photosensitization degradation under visible light irradiation, while its visible-light photoactivity for colorless non-dye organic contaminant was still moderate. Therefore, it is urgently desirable to design an ideal architecture of 2D ultrathin hybrid nanosheets between BiOCl and other narrow band gap semiconductors, aiming to further imbue BiOCl with higher visible-light photocatalytic activity to non-dye organic contaminants.

Graphitic carbon nitrides ( $g\text{-}C_3N_4$ ) has attracted extensive attention as a potential layered-structure photocatalyst with excellent visible-light response due to its narrow band gap of 2.7 eV [21,22]. Since Wang et al. [23] firstly reported that  $g\text{-}C_3N_4$  could be used for hydrogen production from water under visible light irradiation, many followed reports have been booming. However, the photocatalytic performance of bulk  $g\text{-}C_3N_4$  is far from optimum because of its poor mass diffusion and fast charge recombination [24]. Fortunately, these short-comings have been overcome through exfoliating bulk  $g\text{-}C_3N_4$  into  $g\text{-}C_3N_4$  ultrathin nanosheet, which can increase specific surface area, improved electron transport ability along the in-plane direction, and prolong lifetime of photoexcited charge carriers [6,25]. More importantly, it has been reported that when  $g\text{-}C_3N_4$  ultrathin nanosheets were fabricated into 2D/2D heterostructures with other layered semiconductors, its face-to-face contact would form a large interface region, and consequently an enhanced photocatalytic performance would be achieved [26–28]. Nonetheless, to the best of our knowledge, in 2D/2D heterostructures, the insightful understanding of the impact of vacancies on photocatalytic activity is still missing.

Herein, inspired by the above considerations, in this work we have rational designed an oxygen vacancy (OV)-rich ultrathin  $g\text{-}C_3N_4\text{-}BiOCl$  heterostructure nanosheet with a high visible-light-driven photocatalytic activity via a facile solvothermal method. The visible photocatalytic activity of as-prepared ultrathin  $g\text{-}C_3N_4\text{-}BiOCl$  nanosheets was evaluated by the degradation of 4-chlorophenol (4-CP), and several endocrine disruptors (bisphenol A (BPA), bisphenol S (BPS) and bisphenol F (BPF)). Multiple optical and photoelectrochemical experiments were employed to studied the degradation mechanism in this system. The enhanced optical absorption and separation efficiency led to the superior visible-light photocatalytic activity, which were originated from the synergistic effect between oxygen vacancies (OVs) and heterojunction in ultrathin hybrid  $g\text{-}C_3N_4\text{-}BiOCl$  nanosheets. The construction of oxygen vacancy-rich ultrathin 2D/2D heterostructures could bring new opportunities for rational design highly active visible light photocatalysts for environmental remediation and other applications.

## 2. Experimental section

### 2.1. Materials

All chemical reagents used in this work were analytical reagent grade and without further purification. Bismuth nitrate pentahydrate ( $Bi(NO_3)_3\cdot5H_2O$ ), sodium chloride (NaCl), urea, polyvinylpyrrolidone (PVP, K-30), glycerol, 4-chlorophenol (4-CP), bisphenol A (BPA),

bisphenol S (BPS), bisphenol F (BPF) and ethanol were all obtained from Sinopharm Chemical Reagent Co. Ltd. Deionized water was used throughout the experiments.

### 2.2. Catalysts preparation

#### 2.2.1. Synthesis of graphite carbon nitrogen ( $g\text{-}C_3N_4$ ) nanosheets

Bulk  $g\text{-}C_3N_4$  was synthesized by annealing urea at 550 °C for 3 h with the heating rate of 5 °C min<sup>-1</sup> [29]. The  $g\text{-}C_3N_4$  nanosheets were obtained by liquid exfoliating of as-prepared bulk  $g\text{-}C_3N_4$  in water according to the previous reports with a small modification [30]. In detail, 200 mg bulk  $g\text{-}C_3N_4$  powder dispersed in 100 mL water, and then ultrasound for about 4 h. The initial formed suspension was centrifuged at 5000 rpm to remove the residual unexfoliated  $g\text{-}C_3N_4$  nanoparticles and the supernatant was dried at 60 °C for further study. The prepared  $g\text{-}C_3N_4$  nanosheets were denoted as CN.

#### 2.2.2. Synthesis of oxygen vacancy-rich ultrathin $g\text{-}C_3N_4\text{-}BiOCl$ (CN-BC) nanosheets

In a typical procedure, 0.260 g  $g\text{-}C_3N_4$  nanosheets were added in 25 mL water, and then ultrasound for 30 min, yielding a uniform yellow suspension. 0.486 g of  $Bi(NO_3)_3\cdot5H_2O$ , 0.400 g PVP and 25 mL glycerol were dissolved into this suspension at room temperature with vigorous stirring for 1 h. Then, 5 mL saturated NaCl solution was dropwise added into the above mixture. After another 1 h of agitation, the mixture solution was transferred into a 100 mL Teflon-lined stainless steel autoclave. The autoclave was heated at 160 °C for 6 h under autogenous pressure, and then cooled to room temperature naturally. Finally, the resulting product was gathered by centrifugation, washed with water thoroughly and dried at 60 °C, and the obtained powder was ultrathin  $g\text{-}C_3N_4\text{-}BiOCl$  nanosheets with a  $g\text{-}C_3N_4$  loading of 50 wt%. Thereby, a series of  $g\text{-}C_3N_4\text{-}BiOCl$  heterojunction nanosheets with different mass ratios were prepared by adjusting the addition of  $g\text{-}C_3N_4$ . The prepared samples were denoted as xCN-(100-x)BC, where x refers to the percentage of  $g\text{-}C_3N_4$  (x = 0,10,30,50,70,90), which could be abbreviated as BC, 10CN-90BC, 30CN-70BC, 50CN-50BC, 70CN-30BC, and 90CN-10BC.

#### 2.2.3. Synthesis of oxygen vacancy-poor $g\text{-}C_3N_4\text{-}BiOCl$ nanoplates

As a control sample with poor oxygen vacancies, the  $g\text{-}C_3N_4\text{-}BiOCl$  nanoplates with a  $g\text{-}C_3N_4$  loading of 50 wt% were prepared in a similar way without adding PVP, and denoted as 50CN-50BC-P.

### 2.3. Characterization

The micro-morphologies of the samples were observed by using the Quanta 200FEG SEM, FEI Tecnai G2 F30 TEM and JEOL JEM-1400 TEM. XRD patterns were collected by using a Bruker D8 X-ray diffractometer with Cu Ka radiation ( $\lambda = 0.15418$  nm). The thickness of the samples was determined by atomic force microscopy (AFM, Bioscope system, USA). The BET surface area measurements were performed by using an ASAP2020 instrument. The FTIR spectra were recorded on a Perkin-Elmer Spectrum One B spectrometer. X-ray photoelectron spectroscopy measurements were taken on a Thermo ESCALAB 250 with Al Ka X-ray ( $h\nu = 1486.6$  eV) radiation. Electron spin resonance (ESR) spectroscopy (Bruker A200 spectrometer, Germany) was applied for investigation of the existence of oxygen vacancies and the generation of reactive radicals. The UV-vis diffuse reflectance spectra (DRS) of samples were achieved by a spectrophotometer (Shimadzu, UV2550), using the BaSO<sub>4</sub> as the reflectance sample. The steady-state photoluminescence (PL) spectra were obtained using an Hitachi F-4600 fluorescence spectrophotometer with excitation at 315 nm. Total organic carbon (TOC) was analyzed by TOC measuring instrument (Shimadzu TOC-5000). The time-resolved fluorescence emission decay spectra were recorded on an ISS ChronosBH time-domain fluorescence spectrophotometer, and the decay curves were recorded with excitation at 460 nm.

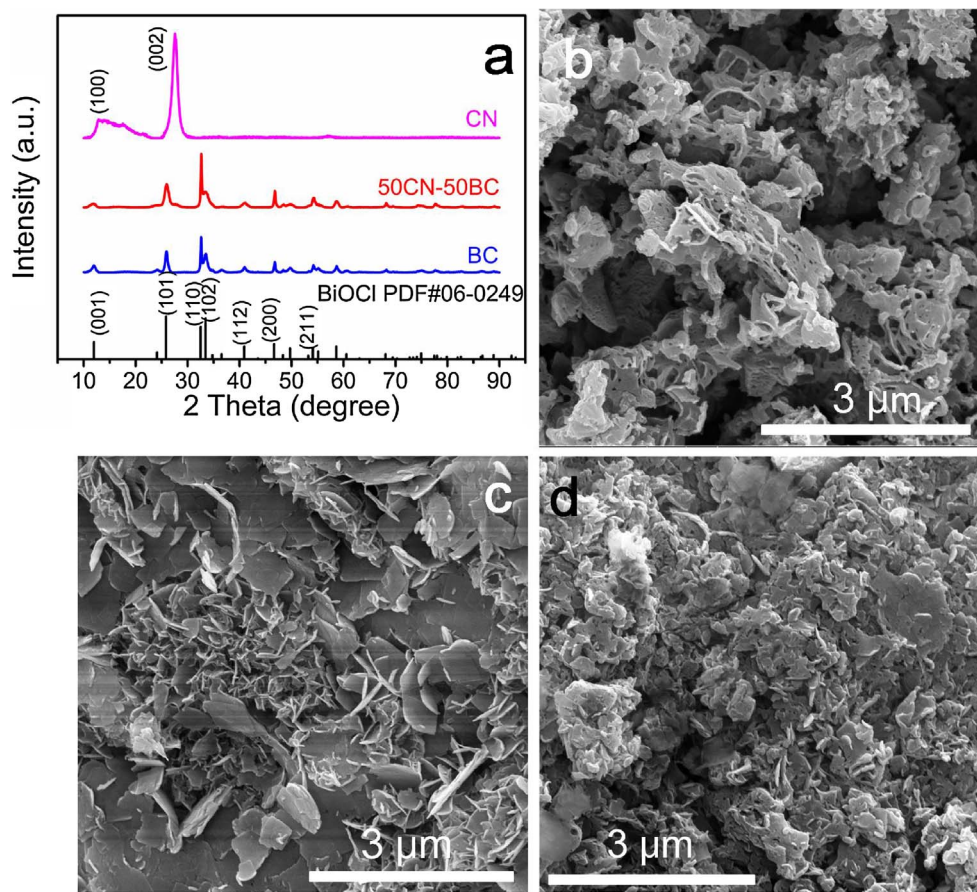


**Fig. 1.** (a) XRD patterns of CN, BC and 50CN-50BC samples. (b-d) SEM images of CN (b), BC (c) and 50CN-50BC heterostructures (d).

#### 2.4. Photocatalytic activity measurement

The visible light photocatalytic activity of all the samples were estimated by measuring the degradation of 4-chlorophenol (4-CP). A 300W short-arc xenon lamp (Perkin-Elmer, PE300BF) equipped with a 420 nm cut-off filter was used as the light source. The reactor was made of open cylindrical Pyrex with diameter 4.5 cm and height 8 cm. The distance between the light source and the surface of the solute was approximately 20 cm. In a typical photocatalytic experiment, the photocatalyst (50 mg) was dispersed in 100 mL of 4-CP solution (10 mg/L), and prior to irradiation, the mixture was stirred for 30 min to reach the adsorption equilibrium in the dark. The temperature of the reactor was maintained at 25 °C by continuous circulating water. At given irradiation time intervals, about 2 mL of the solution was taken out for the analysis of the residual contaminant concentration. The concentration of 4-CP was analyzed by the HPLC system (Waters Baseline 810) with a Waters 486 tunable UV absorbance detector and a Supelco LC-18-DB column (250 mm × 4.6 mm). The HPLC separations were carried out at 280 nm with a mixture of acetonitrile and water in a volume ratio of 70:30 at a flow rate of 1 mL min<sup>-1</sup>. To investigate the generality of as-prepared 50CN-50BC ultrathin nanosheets, several endocrine disruptors (BPA, BPS and BPF) were also degraded in the similar condition of 4-CP. The concentrations of BPA, BPS and BPF were also analyzed by HPLC. The HPLC separations of BPS were detected at 260 nm with a mixture of acetonitrile and water in a volume ratio of 30:70 at a flow rate of 1 mL min<sup>-1</sup>. The HPLC separations of BPA and BPF were detected at 230 nm with a mixture of methanol and water in a volume ratio of 60:40 at a flow rate of 1 mL min<sup>-1</sup>. The intermediate products of 4-CP degradation were measured by using an Ultra Performance Liquid Chromatography tandem mass spectrometry (UPLC-MS, Acquity UPLC-MS) with a triple quadrupole detector (Xevo TQ-S). The negative mode electrospray ionization ((−) ESI) was conducted to analyze the

mass spectra. A 10 μL volume was injected, and the mobile phase was a mixture of acetonitrile and water with a volume ratio of 70:30 at a flow rate of 0.1 mL min<sup>-1</sup>.

#### 2.5. Photoelectrochemical measurement

The transient photo-current measurements and electrochemical impedance spectroscopy (EIS) were performed using an Electrochemical Workstation (660D, Shanghai Chenhua, China). The fabricated photoanodes, a Pt foil, and calomel electrode were used as working, counter and reference electrode, respectively. The working electrodes were prepared by spin-coating method. 5 mg of the photocatalyst powder was suspended in 5 mL of anhydrous ethanol to produce suspension by sonication for 1 h, which was then spin-coated (2000 rpm) onto ITO glass supports. The 0.1 M Na<sub>2</sub>SO<sub>4</sub> aqueous solution was used as the electrolyte. A short-arc xenon lamp (Perkin-Elmer, PE300BF) with a cutoff filter ( $\lambda \geq 420$  nm) was used as the visible light source. The power intensity of the incident light was adjusted to 100 mW cm<sup>-2</sup> by a Si photodiode (Thor Labs).

#### 2.6. Theoretical calculations

In the present work, all the calculations were performed using the periodic density functional theory (DFT) package of Cambridge Serial Total Energy Package (CASTEP) codes. CASTEP is a state-of-the-art quantum mechanics-based program designed specifically for solid-state materials science. The core electrons were treated with the ultrasoft pseudopotential. The exchange-correlation effects of valence electrons were described through the generalized gradient (GGA), within the Perdew-Burke-Ernzerhof (PBE) function. The  $2 \times 2 \times 1$  tetragonal BiOCl supercell (Space group *tP6*, 129) with {001} facet was built and the next calculation process based on this structure. The Monkhorst-

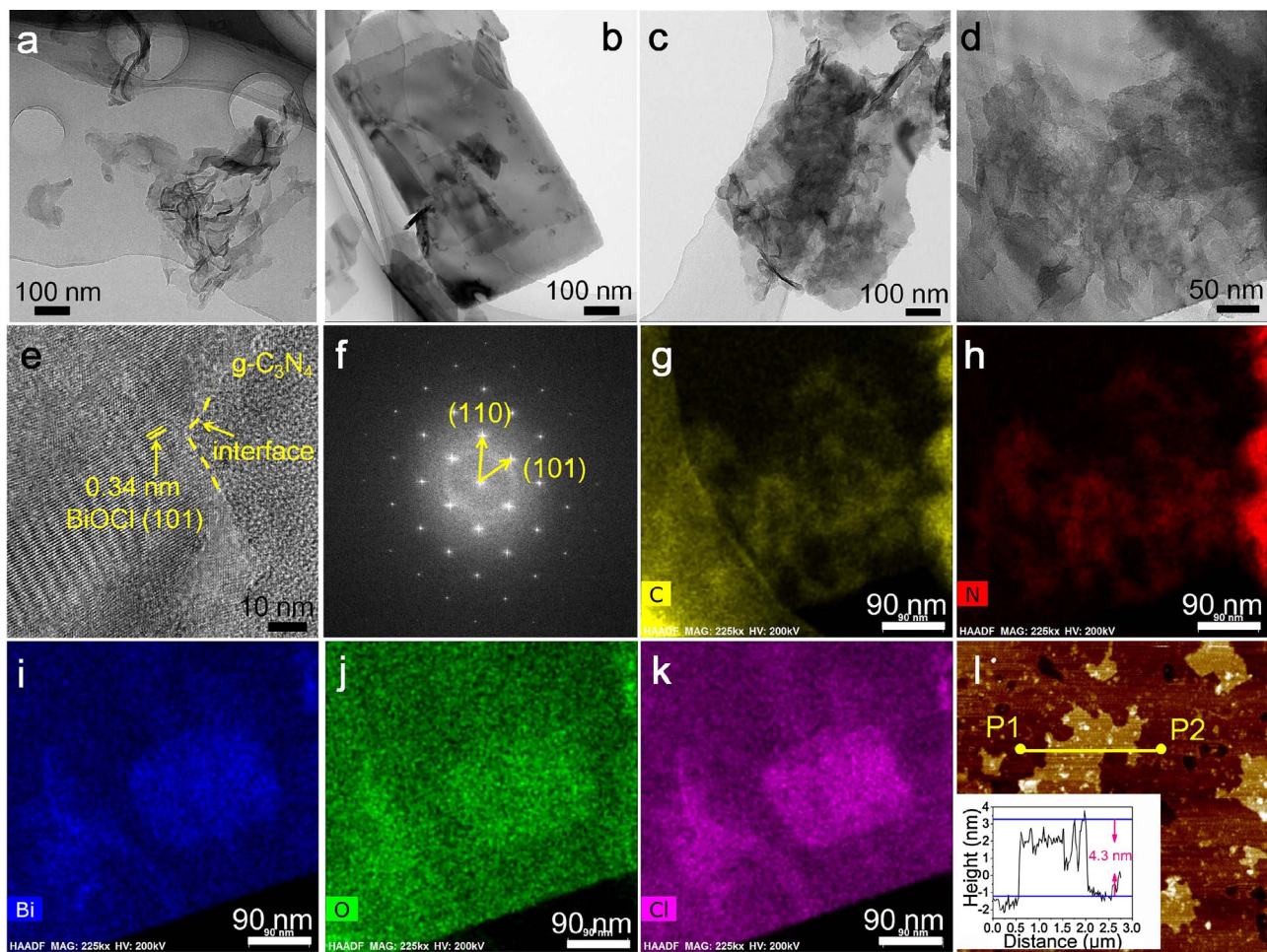


**Fig. 2.** (a-c) Low-magnification of TEM images of CN nanosheets (a), BC nanosheets (b) and 50CN-50BC composite nanosheets (c). (d) High-magnification of TEM image of 50CN-50BC composite nanosheet. (e-f) HRTEM image of 50CN-50BC composite nanosheet (e) and the corresponding FFT image (f). (g-k) The EDS mapping images of 50CN-50BC composite nanosheet. (l) AFM image of 50CN-50BC composite nanosheets and the corresponding height profile shown in the inset of (l).

Pack scheme k-points grid sampling was set as  $4 \times 4 \times 1$  for the irreducible Brillouin zone. The energy cutoff was 450 eV, the convergence criteria were set as the force on the atoms less than  $0.01 \text{ eV } \text{\AA}^{-1}$ , the stress on the atoms less than 0.02 GPa, the atomic displacement less than  $5 \times 10^{-4} \text{ \AA}$ , and the energy change per atom less than  $5 \times 10^{-6} \text{ eV}$ .

### 3. Results and discussion

#### 3.1. Morphology and structure

XRD analysis was carried out to investigate the phase structures of the catalysts. Fig. 1a shows the XRD patterns of CN, BC and 50CN-50BC, and those of other ratio xCN-(100-x)BC samples are shown in Fig. S1. The diffraction peak at  $27.5^\circ$  of CN is a characteristic interlayer stacking reflection of conjugated aromatic systems, which indexes to (002) diffraction planes [31]. The small peak at around  $13.0^\circ$  is indexed to (100) diffraction plane [31]. As for the pure BC nanosheets, all diffraction peaks in this pattern are readily indexed to the tetragonal phase of BiOCl (PDF #06-0249) [32]. As for the ultrathin 50CN-50BC samples, the phases of CN and BC co-exist in the as-prepared CN-BC nano-composite and no other new phases are observed, indicating that the CN-BC hybrids are successfully synthesized. With mass ratio of CN in the xCN-(100-x)BC composites increasing, the peak intensities of the CN increase (Fig. S1), while those of the BC lower gradually.

The morphology and microstructure of the CN-BC samples were characterized by SEM, TEM, HRTEM and EDX-mapping images. SEM

images of ultrathin CN, BC and 50CN-50BC samples are taken and compared in Fig. 1b-d, respectively. The CN sample (Fig. 1b) has a typically layer structure, and the nanosheets as the basic unit appear as loose and soft agglomerates with a size of several micrometers. Similarly, the BC sample (Fig. 1c) demonstrates a nano-slice feature with ultrathin thickness and a typical size ranging from sub-micrometer to several micrometers. Moreover, for the ultrathin 50CN-50BC nanocomposites, a multi-slice structure is displayed with no obvious stacking or aggregation, and the surfaces of BiOCl nanosheets are well covered by two-dimensional g-C<sub>3</sub>N<sub>4</sub> layers.

Fig. 2a is the low-magnification TEM image of the CN nanosheets obtained by liquid exfoliation route from bulk g-C<sub>3</sub>N<sub>4</sub>, and the nearly transparent feature demonstrates its ultrathin thickness. Fig. 2b reveals the as-prepared ultrathin BC nanosheets are rectangle-shaped structures with a smooth surface. For the 50CN-50BC composites (Fig. 2c), the rectangle-shaped nanosheet microstructure is retained, and more importantly, the surface of nanosheet becomes rough, manifesting that the g-C<sub>3</sub>N<sub>4</sub>-BiOCl heterojunction nanosheet is prepared successfully during the solvothermal reaction. Fig. 2d, as a large-scale TEM image of 50CN-50BC, proves that CN nanosheets are well-dispersed on the surface of BC nanosheets with no obvious aggregation, which is consistent with the SEM observations in Fig. 1d. The corresponding HRTEM image (Fig. 2e) exhibits good crystalline and clear lattice fringes with a d-spacing of 0.34 nm corresponding to the (101) planes of the tetragonal BiOCl, which agrees well with the corresponding fast Fourier transform (FFT) pattern results (Fig. 2f). More importantly, the formation of the interface between g-C<sub>3</sub>N<sub>4</sub> layer and BiOCl nanosheet is also presented in

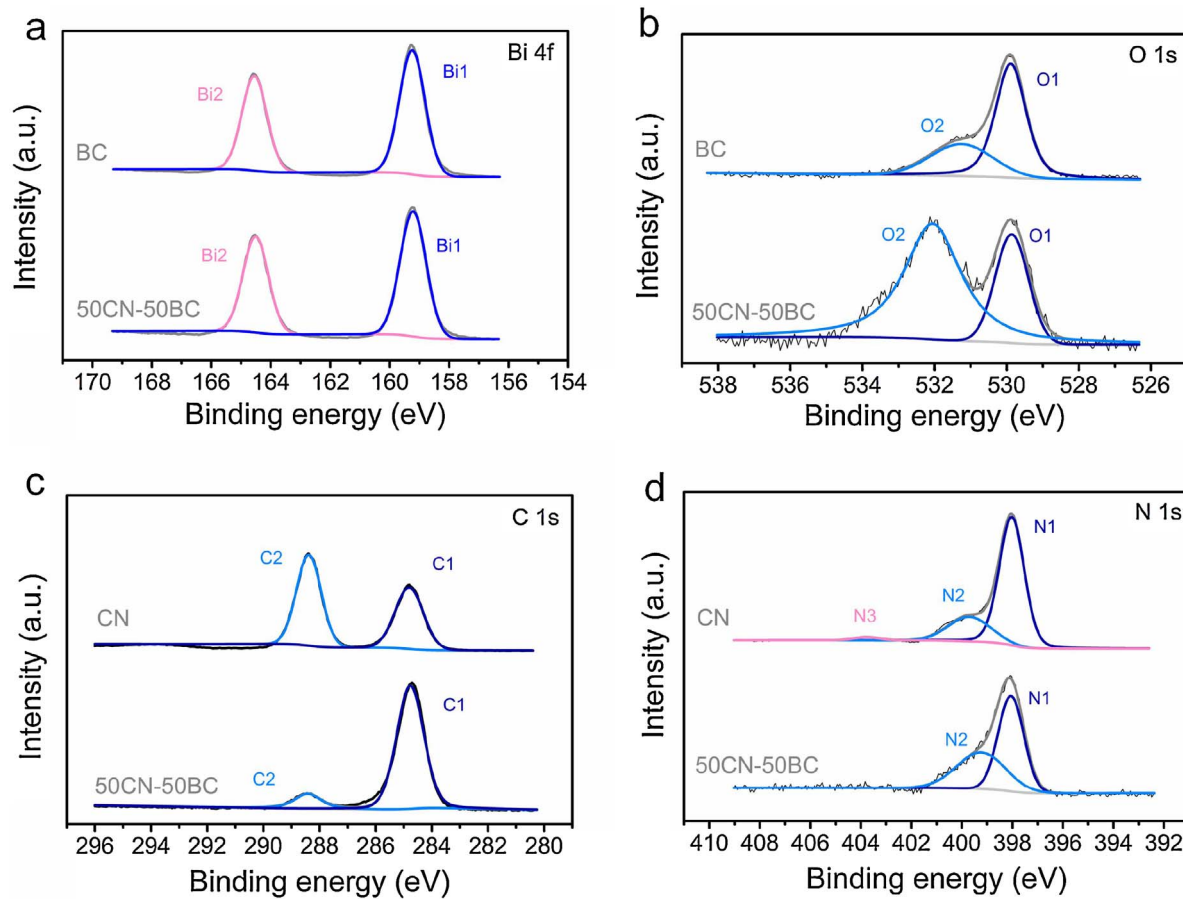


Fig. 3. XPS spectra of 50CN-50BC composite nanosheets: (a) Bi 4f spectrum, (b) O 1s spectrum, (c) C 1s spectrum and (d) N 1s spectrum.

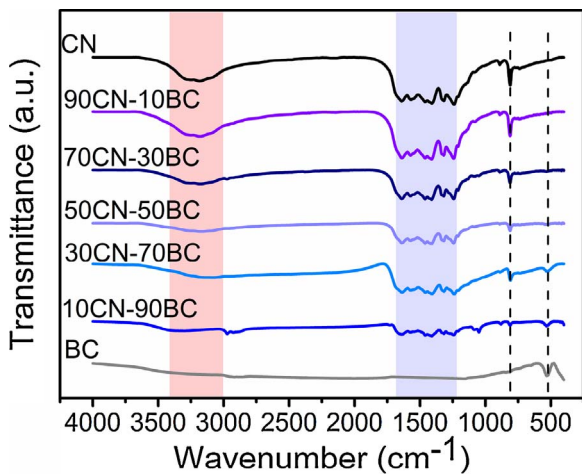


Fig. 4. FTIR spectra of CN, BC and a series of CN-BC heterojunction nanosheets.

Fig. 2e, revealing the strong interfacial interaction between them. As depicted in corresponding EDS mapping images (Fig. 2g–k), it is confirmed that carbon, nitrogen, bismuth, oxygen and chlorine are uniformly distributed over the composite nanosheets. The thickness information of the ultrathin 50CN-50BC nanosheets is obtained from the AFM image, and the corresponding height profile is shown in Fig. 2l. As can be seen, the surface of nanosheet is rough as demonstrated by the TEM images (Fig. 2c and d), which can be further confirmed by the thickness fluctuation determined along the line between Point 1 (P1) and Point 2 (P2) throughout the nanosheet. The thickness of these nanosheets is estimated to be ~4.3 nm.

XPS analysis was performed to investigate the chemical composition of the CN, BC and 50CN-50BC ultrathin composite nanosheets. The high resolution spectra of O 1s, Bi 4f, C 1s and N 1 s are shown in Fig. 3. The binding energy for C 1s peak at 284.8 eV is used as a reference. In Fig. 3a, the peaks at 159.2 eV (Bi1) and 164.5 eV (Bi2) are attributed to Bi 4f<sub>7/2</sub> and Bi 4f<sub>5/2</sub>, which are characteristic of the Bi<sup>3+</sup> in the BiOCl material [33], suggesting that the 50CN-50BC heterostructures do not affect the inter-layered Bi<sup>3+</sup>. Two peaks can also be clearly identified from the O 1s core level spectra as shown in Fig. 3b: O1 peak at 529.9 eV is deemed as the Bi-O bond in the crystal structure of [Bi<sub>2</sub>O<sub>2</sub>]<sup>2+</sup> [34], while O2 peak located at 531.3 and 532.1 eV can be attributed to the O atoms in the vicinity of oxygen vacancies in the BC and 50CN-50BC samples, respectively [35,36]. And the slight O2 peak shift in 50CN-50BC is probably due to the interaction between g-C<sub>3</sub>N<sub>4</sub> and BiOCl in 50CN-50BC sample [37]. As shown in Fig. 3c, the C 1 s spectra for CN and 50BC-50CN both contain two components located at 288.4 (C2) and 284.8 eV (C1), corresponding to N=C=N coordination in the framework of g-C<sub>3</sub>N<sub>4</sub>, and adventitious hydrocarbons, respectively [38]. Meanwhile, the high resolution N 1 s spectra of CN can be deconvoluted into three different peaks at binding energies of 398.0 (N1), 399.7 (N2) and 403.8 eV (N3), respectively (Fig. 3d). The dominant N1 peak is commonly attributed to sp<sup>2</sup> N involved in triazine rings [25,39], while the medium N2 peak is due to bridging N atoms in N-(C) 3 [25,39] or N bonded with H atoms [40]. The very weak N3 peak is assigned to the π-excitations [41]. Importantly, it can be found that there is no change of chemistry shift appeared in 50CN-50BC with respect to CN sample, except for the disappearing of N3 peak. It demonstrates that the coupling of BiOCl with g-C<sub>3</sub>N<sub>4</sub> via an interaction using π-excitations of CN heterocycles, rather than coupled with sole C or N atoms of g-C<sub>3</sub>N<sub>4</sub> [41].

Meanwhile, the chemical structures of the samples were further

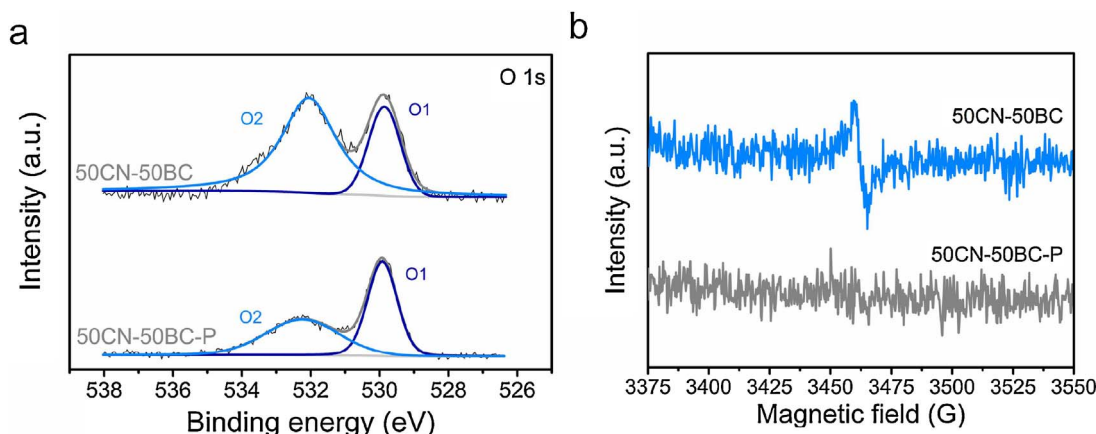


Fig. 5. (a) The high resolution XPS spectra of O 1s and (b) ESR spectra of as-prepared ultrathin 50CN-50BC nanosheets, using 50CN-50BC-P as a reference.

confirmed by the FTIR spectra as shown in Fig. 4. In terms of CN nanosheets, the board peaks between 3000 and 3400 cm<sup>-1</sup> (the red area) correspond to the N–H band. And the peaks at 1240, 1318, 1408, 1570 and 1639 cm<sup>-1</sup> (the blue area) are contributed to the typical stretching modes of CN heterocycles [24]. In addition, the characteristic vibration of triazine rings at 810 cm<sup>-1</sup> is also observed [42]. In regard to the BC nanosheets, the absorption peak at 527 cm<sup>-1</sup> appears, which is assigned to the Bi-O stretching mode [43]. As for the CN-BC hybrids, it is worth noting that the peaks of CN and BC co-exist in the as-prepared CN-BC nanocomposite and no other new phases are observed, manifesting that the CN-BC composite nanosheets are successfully synthesized, which is in agreement with the results of XRD. With mass ratio of CN in the composites increasing, the peak intensities of the CN increase, while those of the BC lower gradually.

Further, the high resolution XPS spectra of O 1s and ESR spectra were employed to identify the oxygen-defective nature of the ultrathin 50CN-50BC nanosheets using 50CN-50BC-P nanoplates (Fig. S2) as a reference. Fig. 5a shows the high resolution O 1s spectra of the two samples. The species of O1 are originated from the lattice oxygen anions, while the species of O2 belong to the oxygen vacancies on the surface, in accordance with Fig. 3b. Notably, there is an obviously increase of O2 peak in 50CN-50BC as compared with that of 50CN-50BC-P, revealing that the as-prepared 50CN-50BC ultrathin nanosheets have a high concentration of surface oxygen vacancies [44]. Meanwhile, the ESR measurement provided fingerprint evidences for probing oxygen vacancies. As shown in Fig. 5b, a sharp signal at  $g = 2.004$ , which is identified as the electrons trapped on oxygen vacancies [45,46], is detected only in 50CN-50BC sample, verifying again that the rich OVs exist in the as-prepared 50CN-50BC ultrathin nanosheets. Besides, the absence of this signal in 50CN-50BC-P sample confirms that there is quite a low concentration of OVs existing in the control sample. Combining with the XPS and ESR characterizations above, we can confirm that the concentration of oxygen vacancies is rich in the ultrathin 50CN-50BC nanosheets, while that is poor in 50CN-50BC-P, providing the prerequisite for investigating the effect of oxygen vacancies on photocatalytic activity in 2D/2D heterostructure.

The optical properties of the as-prepared xCN-(100-x)BC nanosheets were investigated by UV-vis DRS analysis. As depicted in Fig. 6a, the absorption edge of 50CN-50BC composite nanosheets occur a remarkable red-shifting as compared to that of BC, while a slight red-shifting is observed with respect to that of CN. It is indicated that the photo-absorption property of 50CN-50BC composites is slightly superior to that of CN nanosheets, and it is more favorable than BC nanosheets. This result can be ascribed to the 2D/2D heterostructure between CN and BC interface, which mediates the band structure and results in a stronger capacity of light absorption [26]. Furthermore, the absorption edge of 50CN-50BC also possesses a distinct red-shifting with respect to

50CN-50BC-P, corresponded to a band gap narrowing and optical absorption enhancement. This characteristic is due to the overlapping of the OVs' electronic states with the semiconductors' band edge at a high concentration of OVs [11,47]. The corresponding optical band gap energy ( $E_g$ ) can be calculated by the following formula [48,49]:

$a\text{h}\nu = A(\text{h}\nu - E_g)^{n/2}$ , where  $a$ ,  $\text{h}$ ,  $\nu$  and  $A$  represent the absorption coefficient, Planck constant and light frequency and proportionality, respectively. And  $n$  is equal to 4 due to the fundamental absorption of both g-C<sub>3</sub>N<sub>4</sub> and BiOCl is an indirect transition between bands. As shown in Fig. 6b, the optical  $E_g$  of CN, BC, 50CN-50BC and 50CN-50BC-P are estimated to be 2.58, 2.90, 2.45 and 2.55 eV, respectively. The valence band X-ray photoelectron spectra (VB-XPS) were employed to investigate the valence band (VB) of CN and BC nanosheets. According to Fig. 6c, the positions of valence band of CN and BC are found to be at 1.60 and 1.05 eV vs NHE, respectively. According to the equation of  $E_{CB} = E_g - E_{VB}$ , the conduction band (CB) edges of CN and BC are calculated to be -0.98 and -1.85 eV vs NHE, respectively. These data indicate that CN and BC have suitable band potential to construct a heterojunction structure.

To clarify the impact of oxygen vacancies on the band structure, the density-functional calculations of BiOCl with OVs were carried out with consideration of oxygen element exists only in BiOCl. As shown in the band structure (Fig. 6d) and density of states (DOS, Fig. 6e), the Fermi energy level is 0 eV versus the normal hydrogen electrode (NHE). The conduction band and valence band are located above and below the Fermi level, respectively. BiOCl crystal contains an indirect band gap, due to the location of valence band maximum (VBM) and conduction band minimum (CBM) at different k-point [49,50]. The band gap is theoretically calculated to be 2.75 eV, which is slightly lower than the DRS result, as a consequence of the well-known GGA-PBE underestimation [51]. Even more remarkably, there is a sub-band in our calculation results, attributed to the OVs-induced defect level [11], and the band position of this defect level is also confirmed, which is located at 0.74 eV below CBM (Fig. 6d). The existence of defect level can narrow the band gap and increase photoabsorption, which are in good agreement with DRS results. As can be seen in DOS curves (Fig. 6e), the VBM is mainly contributed by the O 2p and Cl 3p states with a small amount of Bi 6s state, and the CBM mainly by the Bi 6p state, which are consistent with previous investigations [52,53].

### 3.2. Photocatalytic activity

Photodegradation of 4-chlorophenol (4-CP) under visible light ( $\lambda > 420$  nm) was used as the probe reaction to evaluate the photocatalytic performance of CN-BC nanosheets. The widespread use of 4-CP and the lack of effective treatment processes have led to its ubiquity in surface waters, which has toxicity to the aquatic organism and ability

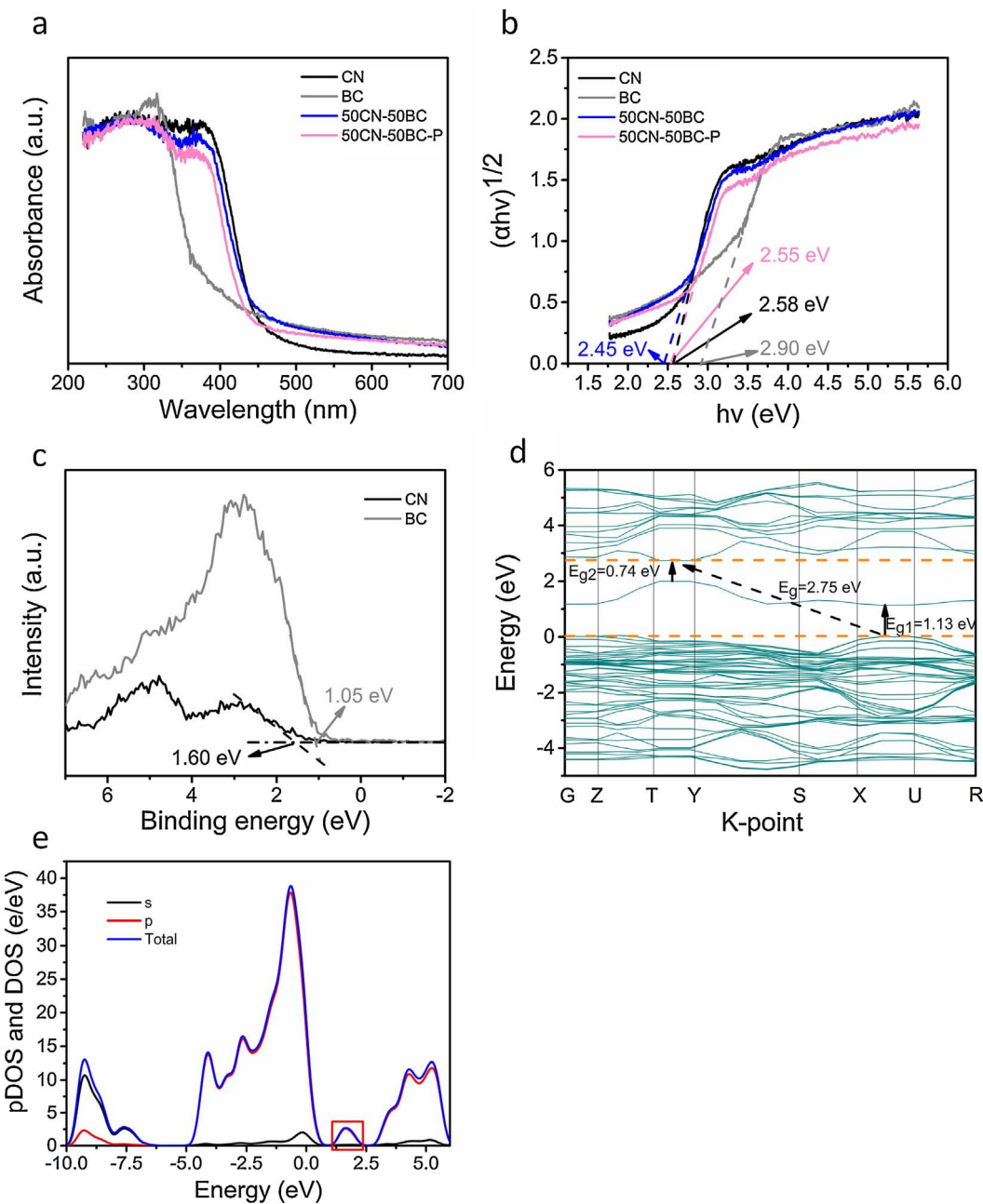


**Fig. 6.** (a) UV-vis diffuse reflection spectra of CN, BC, 50CN-50BC and 50CN-50BC-P. (b) The bandgap value, estimated by a related curve of  $(\alpha h\nu)^{1/2}$  versus photon energy plotted. (c) VB-XPS spectra of CN and BC nanosheets. (d) Band structure and (e) density of states of BC nanosheets with oxygen vacancies.

to bioaccumulate in organisms [54]. Therefore, 4-CP has been regarded as a typical colorless non-dye organic contaminant, and it is of great significance to remove 4-CP from aqueous systems. Without irradiation (Fig. S3), it can be seen that the 4-CP and catalyst suspensions reach absorption-desorption equilibrium at 15 min. And the results indicate that all CN-BC nanosheets show only small amounts of 4-CP adsorption abilities. Under visible-light irradiation, as shown in Fig. 7a, the blank experiment reveals that 4-CP is barely decomposed without photocatalyst. The degradation ratio of 4-CP is 22.7% and 42.6% for pure BC and CN after 120 min, respectively. When CN is coupled with BC, the photodegradation activity is significantly enhanced. The as-prepared 50CN-50BC exhibits the highest activity and nearly 95% of 4-CP can be degraded after 120 min. Nevertheless, when CN and BC are simply mechanical mixed with a mass ratio of 1:1 (denoted as 50CN + 50BC mixed), the activity declines steeply to 32.2%. It further implies that the heterojunction is formed between the interfaces of CN and BC, thus

leading to promoting the photocatalytic performance. Furthermore, in contrast with 50CN-50BC-P, the 50CN-50BC sample with rich OVs exhibits a distinct enhancement on photoactivity, manifesting that surface OVs are conducive to promote photocatalytic performance.

Meanwhile, the degradation data can be further evaluated by the pseudo first-order kinetic equation, as shown in Fig. 7b. The apparent reaction rate constant ( $k$ ) of ultrathin 50CN-50BC nanosheets is calculated as  $0.0250 \text{ min}^{-1}$ , which is 3.4, 5.3 and 12.5 times greater than that of 50CN-50BC-P ( $k = 0.0074 \text{ min}^{-1}$ ), CN ( $k = 0.0047 \text{ min}^{-1}$ ) and BC nanosheets ( $k = 0.0020 \text{ min}^{-1}$ ), respectively. Moreover, in order to further assess the mineralization of 4-CP in water, TOC was detected during the photoreaction process (Fig. S4). After irradiation 120 min, nearly 47% of organic carbon is mineralized over 50CN-50BC, while those were 32%, 25% and 12% over 50CN-50BC-P, CN and BC samples, respectively. All the results clearly exhibit that the OVs-rich 50CN-50BC nanosheets can effectively remove 4-CP as compared to any single

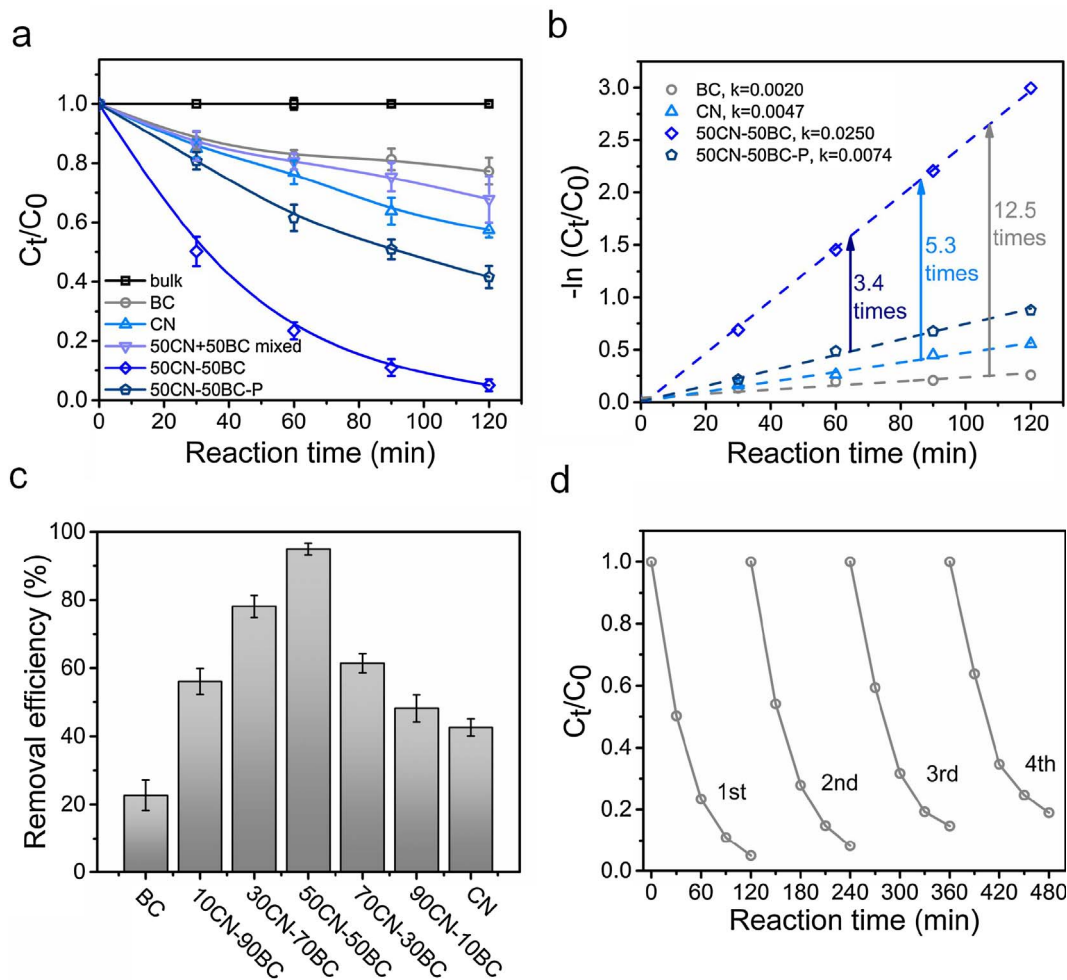


**Fig. 7.** (a) Photocatalytic degradation of 4-CP under visible light irradiation over different samples. (b) Pseudo first-order kinetic fitting and the determined apparent rate constants ( $k$ ). (c) Photocatalytic efficiencies of different  $x$ CN-(100- $x$ )BC samples in the degradation of 4-CP under visible light irradiation. (d) 4-CP removal in the repeated tests over the as-prepared 50CN-50BC.

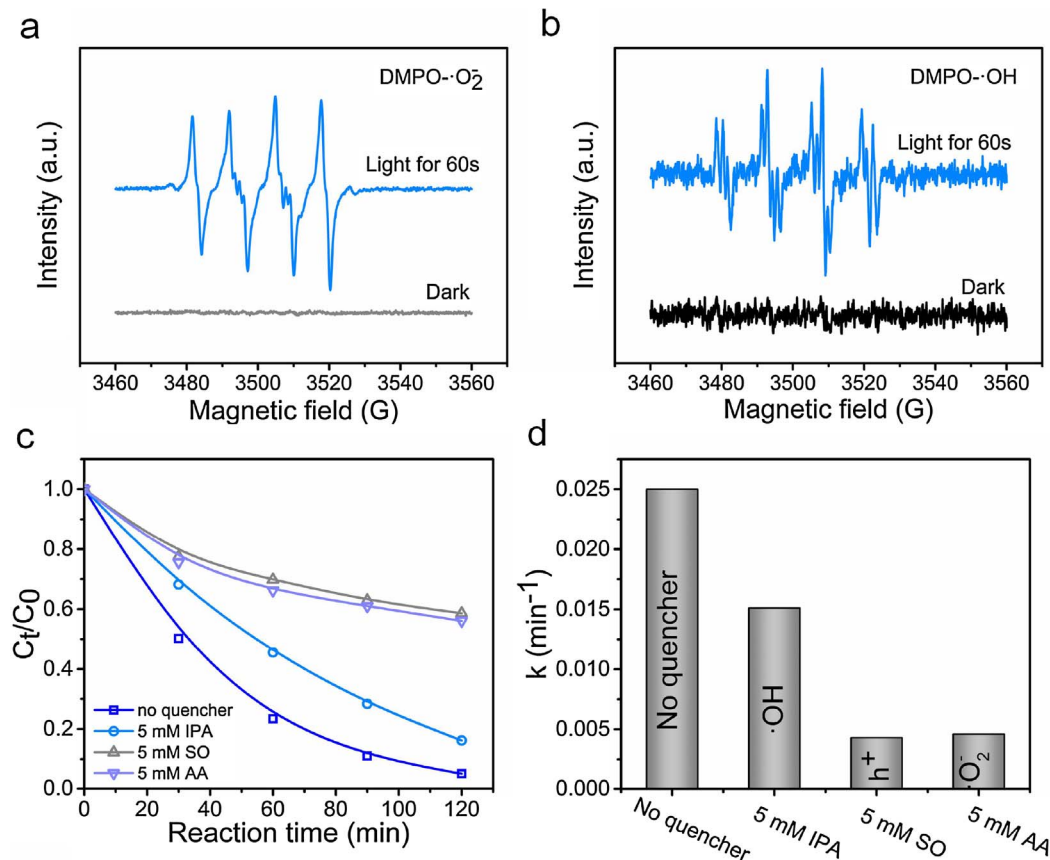
catalyst or the composite with poor OVs. Fig. 7c depicts the degradation ratio of 4-CP over different percentage of CN-BC samples after 120 min irradiation. It can be found that the best content of  $\text{g-C}_3\text{N}_4$  is 50 wt%. Lower or higher content cannot obtain the best photocatalytic activity. This optimization content of  $\text{g-C}_3\text{N}_4$  is consistent with other reported composite photocatalysts [41,55,56], which possibly results from 50%  $\text{g-C}_3\text{N}_4$  restraining the recombination of photoinduced charges more effectively.

Furthermore, the recyclability and physicochemical stability of the ultrathin 50CN-50BC nanosheets in the degradation of 4-CP has been evaluated. In Fig. 7d, the recycling experiment is performed over 50CN-50BC, demonstrating that after four cycles of repeated use, a 4-CP degradation efficiency of 81% is still obtained. Besides, the physicochemical properties of the reused 50CN-50BC nanosheets have been characterized by TEM (Fig. S5a) and XRD images (Fig. S5b), and no obvious variations are found in them. And negligible leakage of bismuth (7  $\mu\text{g/L}$ ) was detected in the reaction solution of 4-CP over 50CN-50BC after 120 min irradiation. These results highlight the excellent recyclability and physicochemical stability of ultrathin 50CN-50BC nanosheets in the photocatalytic degradation of 4-CP. Finally, the ultrathin 50CN-50BC nanosheets also display the generality of degrading other persistence organic contaminants efficiently, such as BPA, BPS and BPF (Fig. S6). Nearly 72% BPS can be degraded within 120 min of visible-light irradiation, and more outstanding, BPA and BPF can be entirely removed within 90 min of visible-light irradiation.

### 3.3. Photocatalytic mechanism in the $\text{g-C}_3\text{N}_4$ -BiOCl system

To evaluate the contribution of the specific oxidative species to this photocatalytic degradation process, ESR measurements and typical scavenger tests were carried out. As shown in Fig. 8a and b, no ESR signals of DMPO- $\cdot\text{O}_2^-$  adduct and DMPO- $\cdot\text{OH}$  adduct are observed in the dark. After visible light irradiation for 60 s, the special spectrum with an intensity ratio of 1:1:1 quartet signal is obviously observed, which is ascribed to the characteristic of DMPO- $\cdot\text{O}_2^-$  adduct [57]. Meanwhile, a four-line ESR signal with the relative intensities of 1:2:2:1 is also obtained, corresponded to the assignment of the DMPO- $\cdot\text{OH}$  adduct [58,59]. These results confirm that  $\cdot\text{O}_2^-$  and  $\cdot\text{OH}$  radicals are both produced in the photodegradation process over 50CN-50BC ultrathin nanosheets. Further, in the scavenger tests, we employed isopropanol (IPA) as the scavenger of  $\cdot\text{OH}$  radicals, ascorbic acid (AA) as the scavenger of  $\cdot\text{O}_2^-$  radicals, and sodium oxalate (SO) as the scavenger of holes ( $\text{h}^+$ ). Fig. 8c shows that when 5 mM AA and 5 mM SO were added into the reaction solution, the degradation efficiency of 4-CP significantly decreased from 95% to 44% and 41%, respectively. On the other hand, the addition of 5 mM IPA slightly decreases the removal efficiency of 4-CP from 95% to 84%. Fig. 8d depicts the corresponding apparent rate constants ( $k$ ) with different quenchers. These results demonstrate that  $\cdot\text{O}_2^-$  and  $\text{h}^+$  are the main active species in the photocatalytic process of CN-BC hybrids, while the  $\cdot\text{OH}$  radicals make a minor contribution to it.

absorption capability and high separation efficiency of electron-hole



pairs are beneficial for the performance of a photocatalyst. Therefore, systematic characterizations have been performed to explore the origination of the superior photoreactivity of 50CN-50BC nanosheets.

Firstly, the surface areas of the catalysts were obtained by using the N<sub>2</sub> adsorption-desorption technology. As shown in Fig. 9a and Table 1, the surface area of CN nanosheets is highest (105.3 m<sup>2</sup> g<sup>-1</sup>), which is higher than that of 50CN-50BC (62.0 m<sup>2</sup> g<sup>-1</sup>), 50CN-50BC-P (60.0 m<sup>2</sup> g<sup>-1</sup>) and BC nanosheets (27.3 m<sup>2</sup> g<sup>-1</sup>). The higher surface area can contribute to providing more active sites, bringing out the enhanced photocatalytic performance. To further explore the intrinsic photoreactivity, apparent reaction rate constant (*k*) was normalized to the surface area, referred to *k<sub>s</sub>*. Table 1 shows that at equivalent mass loadings, it is worth noting that 50CN-50BC exhibits a much higher photoreactivity with *k<sub>s</sub>* = 0.806 × 10<sup>-3</sup> min<sup>-1</sup> L m<sup>-2</sup>, which is 7.0, 5.5 and 3.3 folds greater than that of CN nanosheets (0.114 × 10<sup>-3</sup> min<sup>-1</sup> L m<sup>-2</sup>), BC nanosheets (0.147 × 10<sup>-3</sup> min<sup>-1</sup> L m<sup>-2</sup>) and 50CN-50BC-P nanoplates (0.246 × 10<sup>-3</sup> min<sup>-1</sup> L m<sup>-2</sup>), respectively. These results indicate that 50CN-50BC ultrathin nanosheets show the highest photocatalytic performance, however, its surface area is modest. Therefore, the contribution of surface area can be ruled out from the cause of observed excellent photoreactivity.

Then, the above DRS results (Fig. 6a) indicate that the combination with g-C<sub>3</sub>N<sub>4</sub> nanosheet to form heterostructure can increase the photoabsorption performance of BiOCl nanosheet, however, this cannot entirely explain the reason of significantly high photoactivity of 50CN-50BC. It is because that the photoabsorption ability of 50CN-50BC is similar with that of CN nanosheets; nevertheless, the photocatalytic activity of 50CN-50BC is much higher than that of CN. Meanwhile, in view of the effect of oxygen vacancy, the 50CN-50BC with rich OVs can increase the photoabsorption performance with respect to 50CN-50BC-P with poor OVs [57], which contributes to high photoactivity of 50CN-50BC. Taken together, the enhancement of light absorption capability is possibly the minor reason for the excellent photoactivity of 50CN-50BC.

**Fig. 8.** (a-b) The ESR spectra of DMPO-O<sub>2</sub><sup>-</sup> (a) and DMPO-OH (b) in the presence of 50CN-50BC ultrathin nanosheets under dark and visible light irradiation, respectively. (c) Photocatalytic degradation of 4-CP over 50CN-50BC ultrathin nanosheets under visible light irradiation in the presence of different scavengers. (d) Pseudo first-order kinetic fitting and the determined apparent rate constants (*k*) with different quenchers.

Given the above analysis, we hypothesize that the separation efficiency of electron-hole pairs of the OVs-rich 50CN-50BC possibly much higher than any single component catalyst or composite with OVs-poor, thus leading to its admirable photocatalytic performance. To confirm this speculation, the photoluminescence (PL) and photoelectrochemical analyses were performed to investigate the actual separation and transportation behaviors of the photoexcited charges in these samples. Fig. 9b presents the PL spectra of CN, BC, 50CN-50BC and 50CN-50BC-P at an excitation wavelength of 315 nm. The highest emission intensity of CN nanosheet indicates its fastest recombination rate of electrons and holes. When g-C<sub>3</sub>N<sub>4</sub> coupled with BiOCl nanosheets to form 50CN-50BC hybrids (including 50CN-50BC and 50CN-50BC-P), the PL intensity obviously decreases, suggesting heterostructures can induce more effective separation of photoinduced carriers. Meanwhile, the PL peak of 50CN-50BC is lower than that of 50CN-50BC-P, which indicates that OVs can further inhibit the carriers' recombination, remarkably affecting the lifetime of the carriers and thus enhancing the photocatalytic activity. Under the same irradiation conditions, the PL emission peak of BC nanosheets is lowest, due to the intrinsic low photoresponse and then the formation of relatively low photogenerated electron-hole pairs [60].

Meanwhile, as shown in Fig. 9c, the electrochemical impedance spectra (EIS) of the samples have been measured and compared under visible light irradiation. Normally, the smaller radius in an EIS Nyquist is, the better charge transfer ability would be [61,62]. Namely, the recombination of photogenerated charge carriers would be inhibited, thus enhancing the separation efficiency. In Fig. 9c, the radius of 50CN-50BC nanosheets is visibly smaller than that of 50CN-50BC-P, BC and CN samples, suggesting that 50CN-50BC lead to improved electroconductivity, which are expected to enhance transfer and separation efficiency of photoinduced electron-hole pairs under visible-light irradiation and this would be beneficial for the enhancement of photocatalytic activity. Further, the same results have been obtained in a

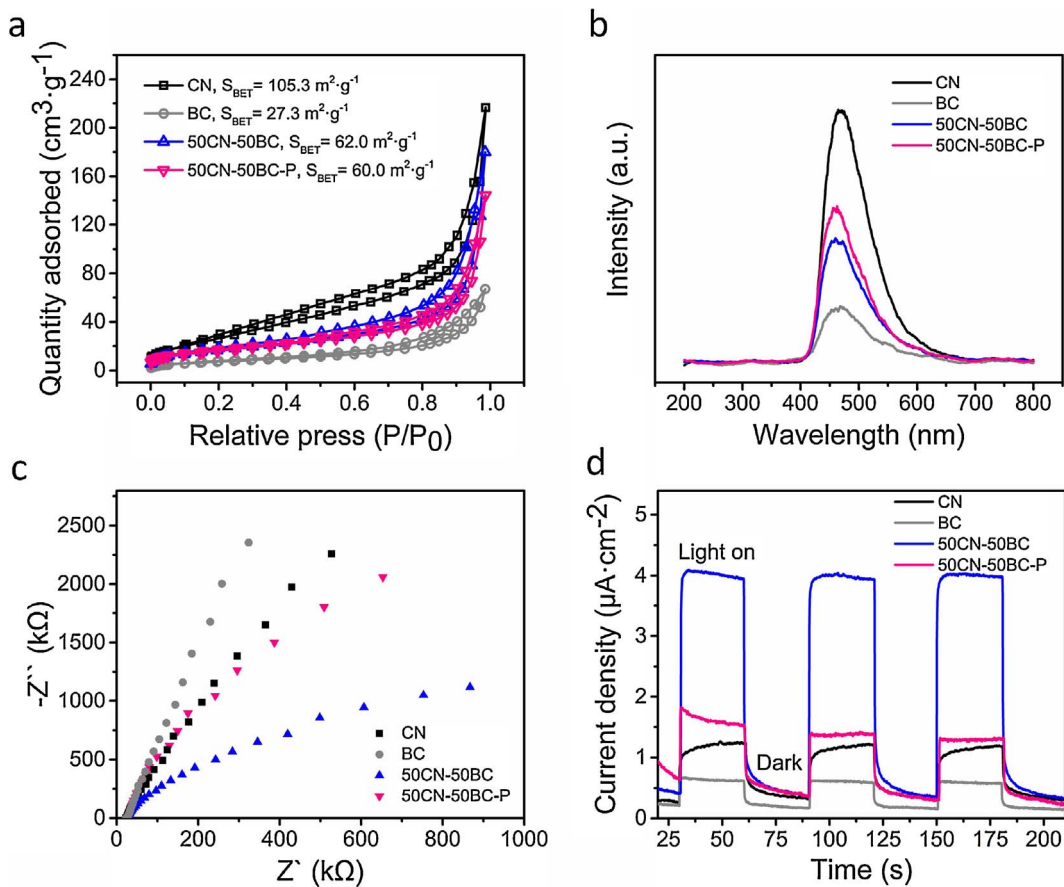


**Fig. 9.** (a) N2 adsorption–desorption isotherms, (b) photoluminescence spectra, (c) electrochemical impedance spectra and (d) transient photocurrent responses of the samples under visible light irradiation.

**Table 1**  
Physicochemical properties of the samples.

Sample description	Reaction rate constant <sup>a</sup> $k$ ( $\times 10^{-3} \text{ min}^{-1}$ )	Surface area <sup>b</sup> ( $\text{m}^2 \cdot \text{g}^{-1}$ )	Normalized reaction rate constants <sup>c</sup> $k_s$ ( $\times 10^{-3} \text{ min}^{-1} \text{ L m}^{-2}$ )
g-C <sub>3</sub> N <sub>4</sub>	4.7	82.7	0.114
BiOCl	2.0	27.3	0.147
50CN-50BC	25.0	62.0	0.806
50CN-50BC-P	7.4	60.0	0.246

<sup>a</sup> Apparent reaction rate constants ( $k$ ) of 4-CP photodegradation on CN-BC architectures were calculated based on the pseudo-first-order model. <sup>b</sup>Surface areas were calculated by Brunauer–Emmett–Teller theory. <sup>c</sup> $k_s$  denoted the rate constant ( $k$ ) normalized to surface area and catalyst concentration,  $k_s = k(\text{catalyst concentration} \times \text{surface area})^{-1}$ .

transient photocurrent response experiment (Fig. 9d). Although all four samples exhibit a quick response to the light either on or off, the generated photocurrent responses are different. Under visible light irradiation, the photocurrent density of 1.5, 1.2 and 0.6  $\mu\text{A} \cdot \text{cm}^{-2}$  can be obtained for 50CN-50BC-P, CN and BC at 0 V vs RHE, respectively. Comparatively, 50CN-50BC has shown a 2.7, 3.4 and 6.8 times higher response value than that of 50CN-50BC-P, CN and BC samples, up to 4.1  $\mu\text{A} \cdot \text{cm}^{-2}$  at the same test condition. This further demonstrates that 50CN-50BC is superior to 50CN-50BC-P, CN and BC in separating electron-hole pairs, which is identified as the mainly reason of its admirable photocatalytic performance [63].

Additionally, to further confirm the enhancement of charge carrier separation efficiency, the analyses of charge carrier lifetime of CN, BC, 50CN-50BC-P and 50CN-50BC were also provided by the time-resolved

fluorescence emission decay spectra with excitation at 460 nm (Fig. 10a). The emission decay curves could be fitted well to a double-exponential function ( $I = A_1 e^{-t/\tau_1} + A_2 e^{-t/\tau_2}$ ), and the fitting results are shown in Table 2. Moreover, an overall comparison of the emission decay behavior is deduced by the intensity-average lifetimes ( $\tau$ ) through the following equation [44]:

$$\tau = \frac{A_1 \tau_1^2 + A_2 \tau_2^2}{A_1 \tau_1 + A_2 \tau_2}$$

The calculation lifetime of 50CN-50BC is 8.340 ns, which is longer than that of CN (7.209 ns), BC (3.477 ns) and 50CN-50BC-P (7.988 ns), respectively. That is to say, the effective electron transport and charge separation efficiency are achieved, manifesting that both heterostructure and OVs are beneficial for photoactivity enhancement, and there is a synergistic effect between them.

Based on above results, the photocatalytic mechanism of OVs-rich 50CN-50BC ultrathin nanosheets can be proposed as follows: On one hand, the heterostructures between g-C<sub>3</sub>N<sub>4</sub> and BiOCl nanosheets can strongly promote the capacity of light absorption and the separation efficiency of photoinduced carriers, thereby enhancing the photocatalytic activity. On the other hand, the large amounts of OVs also can expand the absorbing edge and trap electrons or holes to inhibit the charge carriers' recombination, thus promoting the transfer of these trapped charge carriers to the adsorbates [57,64]. As depicted by schematic diagram (Fig. 10b), the pairs of electrons and holes are photogenerated on the surface of g-C<sub>3</sub>N<sub>4</sub> and BiOCl under visible light irradiation. The electrons ( $e^-$ ) are excited into the CB, and the holes ( $h^+$ ) are remained in VB. Influenced by the effect of heterojunction, the  $h^+$  will transfer to the lower VB of BiOCl. The  $h^+$  cannot directly oxidize the adsorbed H<sub>2</sub>O molecules to ·OH radicals because their

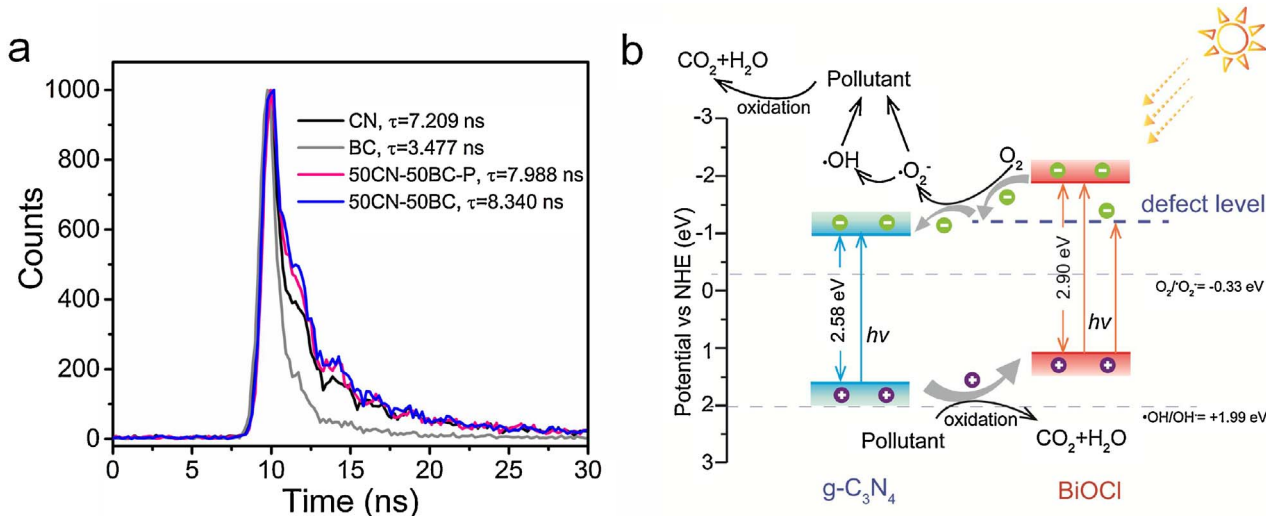


Fig. 10. (a) The time-resolved fluorescence emission decay spectra of CN, BC, 50CN-50BC and 50CN-50BC-P. (b) Schematic illustration of the visible light photocatalytic degradation pollutants over OVs-rich ultrathin 50CN-50BC nanosheets.

Table 2  
Charge carrier lifetime parameters of CN, BC, 50CN-50BC-P and 50CN-50BC samples.

sample	$\tau_1$ (ns)	$\tau_2$ (ns)	A <sub>1</sub> (%)	A <sub>2</sub> (%)	$\tau$
CN	1.4805	8.1184	46.55	53.45	7.209
BC	0.7047	4.0332	53.45	46.55	3.477
50CN-50BC-P	2.0251	9.6407	56.89	43.11	7.988
50CN-50BC	2.3556	10.3522	59.64	40.36	8.340

potential for h<sup>+</sup> is lower than E(OH/OH<sup>-</sup>) (+1.99 eV vs NHE, pH = 7) [65]. Meanwhile, influenced by the effect of heterojunction and OVs, the e<sup>-</sup> of BiOCl will first transfer to the defect level induced by OVs [66], and then transfer to the more positive CB of g-C<sub>3</sub>N<sub>4</sub>. The potential for e<sup>-</sup> is more negative than E(O<sub>2</sub>/O<sub>2</sub><sup>-</sup>) (-0.33 eV vs NHE, pH = 7) [65], which allows the yield of ·O<sub>2</sub><sup>-</sup> radicals via the reduction of dissolved O<sub>2</sub> by e<sup>-</sup>. After that, the ·OH is generated from ·O<sub>2</sub><sup>-</sup> with the assistance of e<sup>-</sup>. Consequently, the active species of ·O<sub>2</sub><sup>-</sup>, ·OH and h<sup>+</sup> can continuously decompose organic contaminants. Therefore, it can be concluded that the synergistic effect between 2D/2D heterojunction and oxygen vacancies promotes the capacity of light absorption, facilitates the efficient separation of photogenerated electron-hole pairs with a prolonged charge lifetime, and thus accelerates the process of photocatalytic reaction.

Besides, in this work, six intermediates including phenol (*m/z* = 93), hydroquinone (*m/z* = 109), maleic acid (*m/z* = 115), crotonyl alcohol (*m/z* = 71), 2,4-dichlorophenol (2,4-DCP, *m/z* = 161) and 2,4,6-trichlorophenol (2,4,6-TCP, *m/z* = 195) were detected by mass spectrometry analyses during the visible-light photocatalytic degradation of 4-CP (*m/z* = 127) over 50CN-50BC for 2 h (Fig. S7-S12). According to these results, the possible transformation pathways have been proposed as exhibited in Fig. S13 [67,68]. Dechlorination and hydroxylation could be the most prominent pathways, which are supported by the main intermediates such as maleic acid and crotonyl alcohol. And the traces of 2,4-DCP and 2,4,6-TCP may derive from the reaction between chlorine radical (·Cl, formed during dechlorination of 4-CP) and 4-CP [67].

#### 4. Conclusion

In this study, we have successfully constructed an oxygen vacancy-rich 2D/2D heterostructure by combining ultrathin BiOCl nanosheets with ultrathin g-C<sub>3</sub>N<sub>4</sub> nanosheets through a facile solvothermal reaction. DRS analysis indicated that the formation of 2D/2D

heterostructures between BiOCl and g-C<sub>3</sub>N<sub>4</sub> nanosheets can enhance the visible-light photoabsorption ability as compared to any single components. XPS and ESR demonstrated the distinct oxygen vacancy concentration in the as-fabricated 50CN-50BC ultrathin nanosheets. DFT calculations revealed that the presence of oxygen vacancies resulted in the appearance of a new defect level, which led to further increasing photoabsorption, also confirmed by DRS. Furthermore, the steady-state PL spectra and photoelectrochemical experiments disclosed that the synergistic effect between 2D/2D heterojunction and oxygen vacancies ensured high photoinduced charge carriers separation efficiency with a prolonged carriers' lifetime, confirmed by the time-resolved fluorescence spectra. Benefiting from the above several advantages, the OVs-rich 50CN-50BC exhibited 95% removal efficiency of 4-CP within 2 h visible light irradiation, which was about 12.5, 5.3 and 3.4 times as that of pure BiOCl, g-C<sub>3</sub>N<sub>4</sub> and OVs-poor 50CN-50BC-P heterostructure, respectively. Also, the catalytic activity for OVs-rich 50CN-50BC did not show any obvious deactivation after four cycles. Our present work provides a new insight on photocatalysts with the synergistic effect between 2D/2D heterojunction and oxygen vacancies to promote the capacity of light absorption, facilitate the efficient separation of photogenerated electron-hole pairs, and thus accelerate the process of photocatalytic reaction in environmental remediation.

#### Acknowledgements

The authors gratefully acknowledge National Natural Science Foundation of China (21304024), State Key Laboratory of Urban Water Resource and Environment in HIT of China (2017TS03), Postdoctoral Science Foundation of Heilongjiang Prov. (LBH-TZ0606 and LBH-Q16012).

#### Appendix A. Supplementary data

Supplementary data associated with this article can be found, in the online version, at <http://dx.doi.org/10.1016/j.apcatb.2017.08.049>.

#### References

- [1] H. Wang, L. Zhang, Z. Chen, J. Hu, S. Li, Z. Wang, J. Liu, X. Wang, Semiconductor heterojunction photocatalysts: design, construction, and photocatalytic performances, Chem. Soc. Rev. 43 (2014) 5234–5244.
- [2] W.J. Ong, L.L. Tan, Y.H. Ng, S.T. Yong, S.P. Chai, Graphitic carbon nitride (g-C<sub>3</sub>N<sub>4</sub>)-Based photocatalysts for artificial photosynthesis and environmental remediation: are we a step closer to achieving sustainability? Chem. Rev. 116 (2016) 7159–7329.
- [3] X. Li, J. Yu, M. Jaroniec, Hierarchical photocatalysts, Chem. Soc. Rev. 45 (2016)

- 2603–2636.
- [4] Y. Li, K. Lv, W. Ho, F. Dong, X. Wu, Y. Xia, Hybridization of rutile  $\text{TiO}_2$  ( $\text{rTiO}_2$ ) with  $\text{g-C}_3\text{N}_4$  quantum dots (CN QDs): An efficient visible-light-driven Z-scheme hybridized photocatalyst, *Appl. Catal. B: Environ.* 202 (2017) 611–619.
- [5] X. Huang, C. Tan, Z. Yin, H. Zhang, 25th anniversary article: hybrid nanostructures based on two-dimensional nanomaterials, *Adv. Mater.* 26 (2014) 2185–2204.
- [6] P. Niu, L. Zhang, G. Liu, H.-M. Cheng, Graphene-Like carbon nitride nanosheets for improved photocatalytic activities, *Adv. Funct. Mater.* 22 (2012) 4763–4770.
- [7] Y. Sun, S. Gao, F. Lei, C. Xiao, Y. Xie, Ultrathin two-dimensional inorganic materials: new opportunities for solid state nanochemistry, *Acc. Chem. Res.* 48 (2015) 3–12.
- [8] P. Niu, L.C. Yin, Y.Q. Yang, G. Liu, H.M. Cheng, Increasing the visible light absorption of graphitic carbon nitride (melon) photocatalysts by homogeneous self-modification with nitrogen vacancies, *Adv. Mater.* 26 (2014) 8046–8052.
- [9] M.K. Nowotny, L.R. Sheppard, T. Bak, J. Nowotny, Defect chemistry of titanium dioxide. application of defect engineering in processing of  $\text{TiO}_2$ -based photocatalysts, *J. Phys. Chem. C* 112 (2008) 5275–5300.
- [10] K. Zhao, L. Zhang, J. Wang, Q. Li, W. He, J.Y. Yin, Surface structure-dependent molecular oxygen activation of  $\text{BiOCl}$  single-crystalline nanosheets, *J. Am. Chem. Soc.* 135 (2013) 15750–15753.
- [11] H. Li, J. Shi, K. Zhao, L. Zhang, Sustainable molecular oxygen activation with oxygen vacancies on the {001} facets of  $\text{BiOCl}$  nanosheets under solar light, *Nanoscale* 6 (2014) 14168–14173.
- [12] J. Li, H. Li, G. Zhan, L. Zhang, Solar water splitting and nitrogen fixation with layered bismuth oxyhalides, *Acc. Chem. Res.* 50 (2017) 112–121.
- [13] X. Zhang, X. Liu, C. Fan, Y. Wang, Y. Wang, Z. Liang, A novel  $\text{BiOCl}$  thin film prepared by electrochemical method and its application in photocatalysis, *Appl. Catal. B: Environ.* 132–133 (2013) 332–341.
- [14] K. Zhang, C. Liu, F. Huang, C. Zheng, W. Wang, Study of the electronic structure and photocatalytic activity of the  $\text{BiOCl}$  photocatalyst, *Appl. Catal. B: Environ.* 68 (2006) 125–129.
- [15] S. Wu, C. Wang, Y. Cui, T. Wang, B. Huang, X. Zhang, X. Qin, P. Brault, Synthesis and photocatalytic properties of  $\text{BiOCl}$  nanowire arrays, *Mater. Lett.* 64 (2010) 115–118.
- [16] S. Peng, L. Li, P. Zhu, Y. Wu, M. Srinivasan, S.G. Mhaisalkar, S. Ramakrishna, Q. Yan, Controlled synthesis of  $\text{BiOCl}$  hierarchical self-assemblies with highly efficient photocatalytic properties, *Chemistry, Asian J.* 8 (2013) 258–268.
- [17] J. Jiang, K. Zhao, X. Xiao, L. Zhang, Synthesis and facet-dependent photoreactivity of  $\text{BiOCl}$  single-crystalline nanosheets, *J. Am. Chem. Soc.* 134 (2012) 4473–4476.
- [18] F. Mushtaq, M. Guerrero, M.S. Sakar, M. Hoop, A.M. Lindo, J. Sort, X. Chen, B.J. Nelson, E. Pellicer, S. Pané, Magnetically driven  $\text{Bi}_2\text{O}_3/\text{BiOCl}$ -based hybrid microrobots for photocatalytic water remediation, *J. Mater. Chem. A* 3 (2015) 23670–23676.
- [19] J. Li, S. Sun, R. Chen, T. Zhang, B. Ren, D.D. Dionysiou, Z. Wu, X. Liu, M. Ye, Adsorption behavior and mechanism of ibuprofen onto  $\text{BiOCl}$  microspheres with exposed {001} facets, *Environ. Sci. Pollut. Res. Int.* 24 (2017) 9556–9565.
- [20] M. Guan, C. Xiao, J. Zhang, S. Fan, R. An, Q. Cheng, J. Xie, M. Zhou, B. Ye, Y. Xie, Vacancy associates promoting solar-driven photocatalytic activity of ultrathin bismuth oxychloride nanosheets, *J. Am. Chem. Soc.* 135 (2013) 10411–10417.
- [21] Y. Li, K. Lv, W. Ho, Z. Zhao, Y. Huang, Enhanced visible-light photo-oxidation of nitric oxide using bismuth-coupled graphitic carbon nitride composite heterostructures, *Chin. J. Catal.* 38 (2017) 321–329.
- [22] S. Fang, Y. Xia, K. Lv, Q. Li, J. Sun, M. Li, Effect of carbon-dots modification on the structure and photocatalytic activity of  $\text{g-C}_3\text{N}_4$ , *Appl. Catal. B: Environ.* 185 (2016) 225–232.
- [23] X. Wang, K. Maeda, A. Thomas, K. Takanabe, G. Xin, J.M. Carlsson, K. Domen, M. Antonietti, A metal-free polymeric photocatalyst for hydrogen production from water under visible light, *Nat. Mater.* 8 (2009) 76–80.
- [24] H. Zhao, H. Yu, X. Quan, S. Chen, Y. Zhang, H. Zhao, H. Wang, Fabrication of atomic single layer graphitic- $\text{C}_3\text{N}_4$  and its high performance of photocatalytic disinfection under visible light irradiation, *Appl. Catal. B: Environ.* 152–153 (2014) 46–50.
- [25] S. Yang, Y. Gong, J. Zhang, L. Zhan, L. Ma, Z. Fang, R. Vajtai, X. Wang, P.M. Ajayan, Exfoliated graphitic carbon nitride nanosheets as efficient catalysts for hydrogen evolution under visible light, *Adv. Mater.* 25 (2013) 2452–2456.
- [26] J. Wang, L. Tang, G. Zeng, Y. Deng, Y. Liu, L. Wang, Y. Zhou, Z. Guo, J. Wang, C. Zhang, Atomic scale  $\text{g-C}_3\text{N}_4/\text{Bi}_2\text{WO}_6$  2D/2D heterojunction with enhanced photocatalytic degradation of ibuprofen under visible light irradiation, *Appl. Catal. B: Environ.* 209 (2017) 285–294.
- [27] C. Tan, X. Cao, X.J. Wu, Q. He, J. Yang, X. Zhang, J. Chen, W. Zhao, S. Han, G.H. Nam, M. Sindoro, H. Zhang, Recent advances in ultrathin two-Dimensional nanomaterials, *Chem. Rev.* (2017).
- [28] Z. Zhang, J. Huang, M. Zhang, Q. Yuan, B. Dong, Ultrathin hexagonal  $\text{SnS}_2$  nanosheets coupled with  $\text{g-C}_3\text{N}_4$  nanosheets as 2D/2D heterojunction photocatalysts toward high photocatalytic activity, *Appl. Catal. B: Environ.* 163 (2015) 298–305.
- [29] D.J. Martin, K. Qiu, S.A. Shevlin, A.D. Handoko, X. Chen, Z. Guo, J. Tang, Highly efficient photocatalytic  $\text{H}_2$  evolution from water using visible light and structure-Controlled graphitic carbon nitride, *Angew. Chem. Int. Ed.* 53 (2014) 9240–9245.
- [30] X. Zhang, X. Xie, H. Wang, J. Zhang, B. Pan, Y. Xie, Enhanced photoresponsive ultrathin graphitic-phase  $\text{C}_3\text{N}_4$  nanosheets for bioimaging, *J. Am. Chem. Soc.* 135 (2013) 18–21.
- [31] P. Qiu, C. Xu, H. Chen, F. Jiang, X. Wang, R. Lu, X. Zhang, One step synthesis of oxygen doped porous graphitic carbon nitride with remarkable improvement of photo-oxidation activity: role of oxygen on visible light photocatalytic activity, *Appl. Catal. B: Environ.* 206 (2017) 319–327.
- [32] M. Guan, C. Xiao, J. Zhang, S. Fan, R. An, Q. Cheng, J. Xie, M. Zhou, B. Ye, Y. Xie, Vacancy associates promoting solar-Driven photocatalytic activity of ultrathin bismuth oxychloride nanosheets, *J. Am. Chem. Soc.* 135 (2013) 10411–10417.
- [33] J. Di, J. Xia, M. Ji, S. Yin, H. Li, H. Xu, Q. Zhang, H. Li, Controllable synthesis of  $\text{Bi}_4\text{O}_3\text{Br}_2$  ultrathin nanosheets for photocatalytic removal of ciprofloxacin and mechanism insight, *J. Mater. Chem. A* 3 (2015) 15108–15118.
- [34] J. Ding, Z. Dai, F. Qin, H. Zhao, S. Zhao, R. Chen, Z-scheme  $\text{BiO}_{1-x}\text{Br}/\text{Bi}_2\text{O}_2\text{CO}_3$  photocatalyst with rich oxygen vacancy as electron mediator for highly efficient degradation of antibiotics, *Appl. Catal. B: Environ.* 205 (2017) 281–291.
- [35] F. Lei, Y. Sun, K. Liu, S. Gao, L. Liang, B. Pan, Y. Xie, Oxygen vacancies confined in ultrathin indium oxide porous sheets for promoted visible-light water splitting, *J. Am. Chem. Soc.* 136 (2014) 6826–6829.
- [36] J. Cheng, Y. Wang, Y. Xing, M. Shahid, W. Pan, Surface defects decorated zinc doped gallium oxynitride nanowires with high photocatalytic activity, *Appl. Catal. B: Environ.* 209 (2017) 53–61.
- [37] F. Wang, W. Li, S. Gu, H. Li, X. Wu, C. Ren, X. Liu, Facile fabrication of direct Z-scheme  $\text{MoS}_2/\text{Bi}_2\text{WO}_6$  heterojunction photocatalyst with superior photocatalytic performance under visible light irradiation, *J. Photochem. Photobiol. A: Chem.* 335 (2017) 140–148.
- [38] H. Yu, R. Shi, Y. Zhao, T. Bian, Y. Zhao, C. Zhou, G.I.N. Waterhouse, L.Z. Wu, C.H. Tung, T. Zhang, Alkali-Assisted synthesis of nitrogen deficient graphitic carbon nitride with tunable band structures for efficient visible-Light-Driven hydrogen evolution, *Adv. Mater.* 29 (2017).
- [39] Y. Cui, J. Zhang, G. Zhang, J. Huang, P. Liu, M. Antonietti, X. Wang, Synthesis of bulk and nanoporous carbon nitride polymers from ammonium thiocyanate for photocatalytic hydrogen evolution, *J. Mater. Chem.* 21 (2011) 13032.
- [40] Y.G. Li, J.A. Zhang, Q.S. Wang, Y.X. Jin, D.H. Huang, Q.L. Cui, G.T. Zou, Nitrogen-Rich carbon nitride hollow vessels: synthesis, characterization, and their properties, *J. Phys. Chem. B* 114 (2010) 9429–9434.
- [41] L. Ye, J. Liu, Z. Jiang, T. Peng, L. Zan, Facets coupling of  $\text{BiOBr-g-C}_3\text{N}_4$  composite photocatalyst for enhanced visible-light-driven photocatalytic activity, *Appl. Catal. B: Environ.* 142–143 (2013) 1–7.
- [42] Y.-P. Yuan, L.-S. Yin, S.-W. Cao, L.-N. Gu, G.-S. Xu, P. Du, H. Chai, Y.-S. Liao, C. Xue, Microwave-assisted heating synthesis: a general and rapid strategy for large-scale production of highly crystalline g- $\text{C}_3\text{N}_4$  with enhanced photocatalytic  $\text{H}_2$  production, *Green Chem.* 16 (2014) 4663–4668.
- [43] K. Wang, C. Shao, X. Li, X. Zhang, N. Lu, F. Miao, Y. Liu, Hierarchical heterostructures of p-type  $\text{BiOCl}$  nanosheets on electrospun n-type  $\text{TiO}_2$  nanofibers with enhanced photocatalytic activity, *Catal. Commun.* 67 (2015) 6–10.
- [44] J. Wang, Y. Xia, H. Zhao, G. Wang, L. Xiang, J. Xu, S. Komarneni, Oxygen defects-mediated Z-scheme charge separation in  $\text{g-C}_3\text{N}_4/\text{ZnO}$  photocatalysts for enhanced visible-light degradation of 4-chlorophenol and hydrogen evolution, *Appl. Catal. B: Environ.* 206 (2017) 406–416.
- [45] W. Bi, C. Ye, C. Xiao, W. Tong, X. Zhang, W. Shao, Y. Xie, Spatial location engineering of oxygen vacancies for optimized photocatalytic  $\text{H}_2$  evolution activity, *Small* 10 (2014) 2820–2825 (2742).
- [46] J. Hou, S. Cao, Y. Wu, F. Liang, Y. Sun, Z. Lin, L. Sun, Simultaneously efficient light absorption and charge transport of phosphate and oxygen-vacancy confined in bismuth tungstate atomic layers triggering robust solar  $\text{CO}_2$  reduction, *Nano Energy* 32 (2017) 359–366.
- [47] I. Justicia, P. Ordejón, G. Canto, J.L. Mozos, J. Fraxedas, G.A. Battiston, R. Gerbasi, A. Figueras, Designed self-doped titanium oxide thin films for efficient visible-light photocatalysis, *Adv. Mater.* 14 (2002) 1399–1402.
- [48] Z. Wan, G. Zhang, X. Wu, S. Yin, Novel visible-light-driven Z-scheme  $\text{Bi}_{12}\text{GeO}_{20}/\text{g-C}_3\text{N}_4$  photocatalyst: oxygen-induced pathway of organic pollutants degradation and proton assisted electron transfer mechanism of Cr(VI) reduction, *Appl. Catal. B: Environ.* 207 (2017) 17–26.
- [49] G. Liu, S. You, M. Ma, H. Huang, N. Ren, Removal of nitrate by photocatalytic denitrification using nonlinear optical material, *Environ. Sci. Technol.* 50 (2016) 11218–11225.
- [50] G. Wang, H. Chen, Y. Li, A. Kuang, H. Yuan, G. Wu, A hybrid density functional study on the visible light photocatalytic activity of (Mo, Cr)-N codoped KNbO(3), *Phys. Chem. Chem. Phys.* 17 (2015) 28743–28753.
- [51] J. Zhang, S. Wageh, A. Al-Ghamdi, J. Yu, New understanding on the different photocatalytic activity of wurtzite and zinc-blende CdS, *Appl. Catal. B: Environ.* 192 (2016) 101–107.
- [52] X. Zhang, C. Fan, Y. Wang, Y. Wang, Z. Liang, P. Han, DFT + U predictions: the effect of oxygen vacancy on the structural, electronic and photocatalytic properties of Mn-doped  $\text{BiOCl}$ , *Comput. Mater. Sci.* 71 (2013) 135–145.
- [53] H. Zhang, L. Liu, Z. Zhou, Towards better photocatalysts: first-principles studies of the alloying effects on the photocatalytic activities of bismuth oxyhalides under visible light, *Phys. Chem. Chem. Phys.* 14 (2012) 1286–1292.
- [54] Z. Ai, P. Yang, X. Lu, Degradation of 4-chlorophenol by microwave irradiation enhanced advanced oxidation processes, *Chemosphere* 60 (2005) 824–827.
- [55] L. Ge, C. Han, J. Liu, Novel visible light-induced  $\text{g-C}_3\text{N}_4/\text{Bi}_2\text{WO}_6$  composite photocatalysts for efficient degradation of methyl orange, *Appl. Catal. B: Environ.* 108–109 (2011) 100–107.
- [56] H. Yan, H. Yang,  $\text{TiO}_2\text{-g-C}_3\text{N}_4$  composite materials for photocatalytic  $\text{H}_2$  evolution under visible light irradiation, *J. Alloys Compd.* 509 (2011) 26–29.
- [57] H. Li, J. Li, Z. Ai, F. Jia, L. Zhang, Oxygen vacancy-Mediated photocatalysis of  $\text{BiOCl}$ : reactivity, selectivity and perspective, *Angewandte Chemie* (2017), <http://dx.doi.org/10.1002/ange.201705628>.
- [58] P. Qiu, C. Xu, H. Chen, F. Jiang, X. Wang, R. Lu, X. Zhang, One step synthesis of oxygen doped porous graphitic carbon nitride with remarkable improvement of photo-oxidation activity: role of oxygen on visible light photocatalytic activity, *Appl. Catal. B: Environ.* 206 (2017) 319–327.
- [59] P. Shao, Z. Ren, J. Tian, S. Gao, X. Luo, W. Shi, B. Yan, J. Li, F. Cui, Silica hydrogel-

- mediated dissolution-recrystallization strategy for synthesis of ultrathin (-Fe<sub>2</sub>O<sub>3</sub>) nanosheets with highly exposed (110) facets: a superior photocatalyst for degradation of bisphenol S, *Chem. Eng. J.* 323 (2017) 64–73.
- [60] J. Liqiang, Q. Yichun, W. Baiqi, L. Shudan, J. Baojiang, Y. Libin, F. Wei, F. Honggang, S. Jiazhong, Review of photoluminescence performance of nano-sized semiconductor materials and its relationships with photocatalytic activity, *Sol. Energy Mater. Sol. Cells* 90 (2006) 1773–1787.
- [61] Y. Hou, F. Zuo, A. Dagg, P. Feng, Visible light-driven alpha-Fe<sub>2</sub>O<sub>3</sub> nanorod/graphene/BiV<sub>1-x</sub>Mo<sub>x</sub>O<sub>4</sub> core/shell heterojunction array for efficient photoelectrochemical water splitting, *Nano Lett.* 12 (2012) 6464–6473.
- [62] N.J. Bell, Y.H. Ng, A. Du, H. Coster, S.C. Smith, R. Amal, Understanding the enhancement in photoelectrochemical properties of photocatalytically prepared TiO<sub>2</sub>-Reduced graphene oxide composite, *J. Phys. Chem. C* 115 (2011) 6004–6009.
- [63] Y. He, L. Zhang, B. Teng, M. Fan, New application of Z-scheme Ag<sub>3</sub>PO<sub>4</sub>/g-C<sub>3</sub>N<sub>4</sub> composite in converting CO<sub>2</sub> to fuel, *Environ. Sci. Technol.* 49 (2015) 649–656.
- [64] H. Li, J. Shang, Z. Ai, L. Zhang, Efficient visible light nitrogen fixation with BiOBr nanosheets of oxygen vacancies on the exposed {001} facets, *J. Am. Chem. Soc.* 137 (2015) 6393–6399.
- [65] X. Hu, J. Tian, Y. Xue, Y. Li, H. Cui, Bi<sub>2</sub>WO<sub>6</sub> nanosheets decorated with Au nanorods for enhanced near-Infrared photocatalytic properties based on surface plasmon resonance effects and wide-Range near-Infrared light harvesting, *ChemCatChem* 9 (2017) 1511–1516.
- [66] J. Jiang, L. Zhang, H. Li, W. He, J.J. Yin, Self-doping and surface plasmon modification induced visible light photocatalysis of BiOCl, *Nanoscale* 5 (2013) 10573.
- [67] H. Ji, F. Chang, X. Hu, W. Qin, J. Shen, Photocatalytic degradation of 2,4,6-trichlorophenol over g-C<sub>3</sub>N<sub>4</sub> under visible light irradiation, *Chem. Eng. J.* 218 (2013) 183–190.
- [68] M. Humayun, Y. Qu, F. Raziq, R. Yan, Z. Li, X. Zhang, L. Jing, Exceptional visible-Light activities of TiO<sub>2</sub>-Coupled N-Doped porous perovskite LaFeO<sub>3</sub> for 2,4-Dichlorophenol decomposition and CO<sub>2</sub> conversion, *Environ. Sci. Technol.* 50 (2016) 13600–13610.